Supporting Information for

Tuning Intermediate Binding Enables Selective Electroreduction of Carbon Dioxide to Carbon Monoxide on Copper-Indium Catalyst

Shengzhou Xu,[a] Chenglong Wang,[a] Chunjing Ran,[a] Hexing Yang,[a] Wangjiang Gao,[a] Bitao Dong,*[b] Yuhang Liu,[c] and Dan Ren*[a]

a. School of Chemical Engineering and Technology, Xi'an Jiaotong University, West Xianning Road 28, Xi'an 710049, China

b. Department of Materials Sciences and Engineering, Division of Solid State Physics, Angstrom Laboratory, Uppsala University, Uppsala, SE-75105, Sweden

c. School of Materials Science and Engineering, Xi'an Jiaotong University, West Xianning Road 28, Xi'an 710049, China

**Correspondence shall be addressed to dongbitao0023@outlook.com or dan.ren@xjtu.edu.cn*

Table of Contents

S1. Experimental Details

Preparation of the electrolyte and electrode

Deionized water (18.2 MΩ cm, Prima-S15UV, HHitech) was used for the preparation of electrolyte and the washing of glassware. 3 M KOH was prepared by dissolving 86.165 g KOH (95%, Shanghai Macklin) in 500 mL deionized water. The electrolyte, 0.5 M $KHCO_3$, was prepared by dissolving 25.03 g $KHCO_3$ (99.99%, Shanghai Macklin) into 500 mL deionized water.

Polycrystalline Cu layer with an average thickness of 900 nm was first coated onto the surface of commercial gas diffusion electrode (GDE, Sigracet 38BC, Fuel Cell Store) via sputtering (MSP-300B, Beijing Chuangshiweina Technology Co., Ltd). Cu target (99.99%) purchased from ZhongNuo Advanced Material (Beijing) Technology Co., Ltd was bombarded under a direct current mode with a power of 50 W, corresponding to a deposition rate of 0.35 nm s^{-1}. The pressure of the chamber during deposition was maintained below 9×10^{-3} Pa. The sputtered Cu/GDE was then anodized at a constant geometric current density of 8 mA cm^{-2} (DH7000C, DHtest) in 3 M KOH using a two-electrode configuration with a carbon rod as the counter electrode. The anodization treatment continued till the voltage reached a threshold of 2.1 V. After the anodization, the resulting $Cu(OH)_2$ film was thoroughly rinsed with deionized water and dried naturally. The film was then annealed at 150 °C for 1 hr under ambient atmosphere, leading to the formation of uniform CuO nanowires (NWs).

In film with various thickness, ranging from 0.5 to 60 nm, was coated onto Cu NWs to form CuO-In-X via sputtering using an In target (99.995%), where X represents the thickness of In film. The sputtering was performed under a direct current mode with a power of 30 W, corresponding to a deposition rate of 1.45 nm s^{-1}. The In/GDE samples were also prepared via sputtering, with a film thickness of 1000 nm. Pt layer with a thickness of 100 nm was coated onto the surface of commercial PTFE layer (Hebei Zhongxing Weiye Experimental Instrument Co., Ltd) via sputtering from a Pt target (99.99%). The sputtering was performed under a direct current mode with a power of 50 W, corresponding to a deposition rate of 0.17 nm s^{-1}.

Material characterization

The crystalline structure of the films was analyzed by an X-ray diffractometer (XRD Shimadzu XRD-6100) using Cu *Kα* radiation. Diffractograms were recorded between 2θ = 10 to 80° at a scan

rate of 10° min^{-1} and a step size of 0.015°. The surface morphology of the catalysts was characterized by a field emission scanning electron microscope (FE-SEM, Tescan Mira4). Elemental distribution maps were obtained by energy dispersive X-ray spectroscopy (EDX, Oxford Xplore30). X-ray photoelectron spectroscopy (XPS) was performed using an AXIS SUPRA+ instrument (Shimadzu) with an aluminum target. Transmission electron microscopy (TEM) was performed on a JEM-F200 (JEOL) instrument, equipped with a high-angle angular dark field (HAADF) detector. The inductively coupled plasma mass spectrometry (ICP-MS) analysis was really carried out on an iCAP Q (Thermo Fisher) instrument and analyzed the metal element content in the electrolyte. The samples of TEM were prepared as follows. The catalyst film was first scraped off the GDE substrate with a disposable needle and then suspended in isopropyl alcohol (99.5%, Macklin). After 5 minutes of sonication, the suspension was dropped on a Au grid coated with a thin layer of carbon film (200 mesh, Xi'an Zhongjingkeyi EM Technology Co., Ltd.) and then dried naturally under ambient atmosphere. Temperature-programmed desorption (TPD) was performed on BeiShiDe Instrument (BSD-Chem C200).

Electrochemical reduction of CO_2 or CO

The electroreduction of CO_2/CO was carried out in a custom-built 3-electrode electrochemical flow cell. The flow electrolytic cell consists of four compartments, namely the gas chamber and liquid chamber of the cathode, and the gas chamber and liquid chamber of the anode. The catholyte chamber and anolyte chamber were separated by a piece of anion exchange membrane (AEM, Fumasep FKS-50). A KCl-saturated Ag/AgCl (Shanghai CHInstruments Co.) was used as the reference electrode. Pt/PTFE was used as the counter electrode. The working electrode is CuO-In/GDE or CuO/GDE or In/GDE. Aqueous $KHCO_3$ (99.99%, Macklin) solution with a concentration of 0.5 M was flowed into the anolyte chamber and catholyte chamber at a rate of 0.15 cm^3 min^{-1}, controlled by a peristaltic pump (ipump2s, Signal). CO_2 or CO (99.999%, Henan Yuanzheng Special Gas Co.) was infused into the cathodic chamber with a flow rate of 15 cm^3 min^{-1}, controlled by a mass flow controller (MC-100SCCM, Alicat Scientific). Chronopotentiometry (CHI604E, Shanghai CHInstruments Co.) was applied to the electrochemical cell for 1000s, with the products being quantified by gas chromatography and liquid chromatography.

Electrochemical adsorption of *CO and *OH

0.5 M $KHCO_3$ solution was pumped into the anolyte and catholyte chamber, respectively, by the peristaltic pump at a rate of 0.15 cm^3 min^{-1}. CO or N_2 (99.999%, Henan Yuanzheng Special Gas Co.) was infused into the cathodic gas chamber at a flow rate of 50 cm^3 min^{-1}, controlled by the mass flow controller. Galvanostatic treatment was applied to the catalyst at a current density of -20 mA cm^{-2} for 60 s before the start of each test. A wide potential window from -2.97 V to +2.03 V vs. Ag/AgCl was selected to measure the oxidation and reduction peaks. Then the potential window was tuned to a narrow range from -1.07 V to -0.57 V vs. Ag/AgCl, to characterize the *CO adsorption and stripping behavior.

For *OH adsorption, the electrodes were pre-treated at -30 mA cm^{-2} for 60 s to remove possible surface oxides. Cyclic voltammetry was then applied to the working electrode in a N_2-saturated 1 M KOH solution. The curves were recorded within a potential range from -0.67 to 0.03 V versus Ag/AgCl at a scan rate of 100 mV s^{-1}. N_2 was flowed into the cathodic chamber with a flow rate of 15 cm^3 min^{-1}, controlled by a mass flow controller (MFC-100SCCM, Alicat Scientific). All the measurements were carried out in the same flow cell.

Double layer capacitance measurement

The electrochemical active surface areas and roughness factors of Cu and Cu-In catalysts were assessed by measuring their double layer capacitance values in the flow cell. Aqueous $KHCO_3$ solution with a concentration of 0.5 M was pumped into the anodic and cathodic electrolyte chamber, respectively, by the peristaltic pump at a rate of 0.15 cm^3 min^{-1}. N_2 was flowed into cathodic and anodic chambers, respectively, at a flow rate of 15 cm^3 min^{-1}. Cyclic voltammograms were recorded at different scan rates in a non-Faradaic potential range. The double-layer capacitance of GDE was also measured in an H-cell and the electrolyte used was 0.5 M aqueous $KHCO_3$ solution. Carbon rod was used as the counter electrode.

***In situ* Raman spectroscopy**

In situ Raman spectroscopy was carried out in a custom-built spectro-electrochemical PEEK cell using a confocal Raman spectrometer (RTS-2, Zolix). A KCl-saturated Ag/AgCl was used as the reference electrode. A piece of anion exchange membrane was used to separate the catholyte chamber

and anolyte chamber to avoid the diffusion of cations, which might affect the acquired spectrum. A near-infrared diode laser (785 nm, Zolix) was used as the excitation source. A water immersion objective lens (60×, Olympus) was used for focusing and collecting the scattered signal. The electrochemical CO_2 reduction was performed at open circuit potential as well as at different current density from -10 to -90 mA cm^{-2} in 0.5 M $KHCO_3$. Multiple spectra were collected at the steady state and one representative spectrum at each current density was shown without any post-treatment, such as background smoothing or cosmic peak removing.

Solar-driven electrochemical CO_2 reduction

The solar-driven CO_2 reduction system was engineered by wiring the solar cell with the electrolyzer. The solar cell employed here was a triple-junction $InGaP_2$/InGaAs/Ge photovoltaic cell, with an effective illumination area of 0.92 cm^2. During test, the solar simulator was illuminated under standard air mass (AM)1.5G light, the intensity of which was calibrated. The *j*-V characteristics of the solar cell were assessed at a scan rate of 10 mV s^{-1} within the voltage range of 0 V to open circuit potential. The electrolyzer was a customized two-electrode flow cell with IrO_x as the counter electrode. 2 M KOH was used as the electrolyte. The thickness of the In loading was also adjusted to 90 nm. The *j*-V behavior was recorded at a scan rate of 10 mV s^{-1} at an applied potential of 0.3 to 2.5 V. The full system was also illuminated continuously, with the generated gas products periodically sampled into the GC for quantification.

Calculation on the free Gibbs energy

For the given equation: $2In(s) + 3CuO(s) \leftrightharpoons In_2O_3(s) + 3Cu(s)$, the free Gibbs energy change is calculated based of formation Gibbs free energy of each chemical via software *Research Equations*.

DFT calculation

We used the DFT as implemented in the Vienna Ab initio simulation package (VASP) in all calculations. The exchange-correlation potential is described by using the generalized gradient approximation of Perdew-Burke-Ernzerhof (GGA-PBE). The projector augmented-wave (PAW) method is employed to treat interactions between ion cores and valence electrons. The plane-wave cutoff energy was fixed to 500 eV. Given structural models were relaxed until the Hellmann–Feynman forces smaller than -0.02 eV/Å and the change in energy smaller than 10^{-5} eV was attained. The vacuum

thickness was set to be 15 Å to minimize interlayer interactions. During the relaxation, the Brillouin zone was represented by a Γ centered k-point grid of 7×7×1. Grimme's DFT-D3 methodology was used to describe the dispersion interactions among all the atoms in adsorption models.

S2. Additional Materials Characterizations

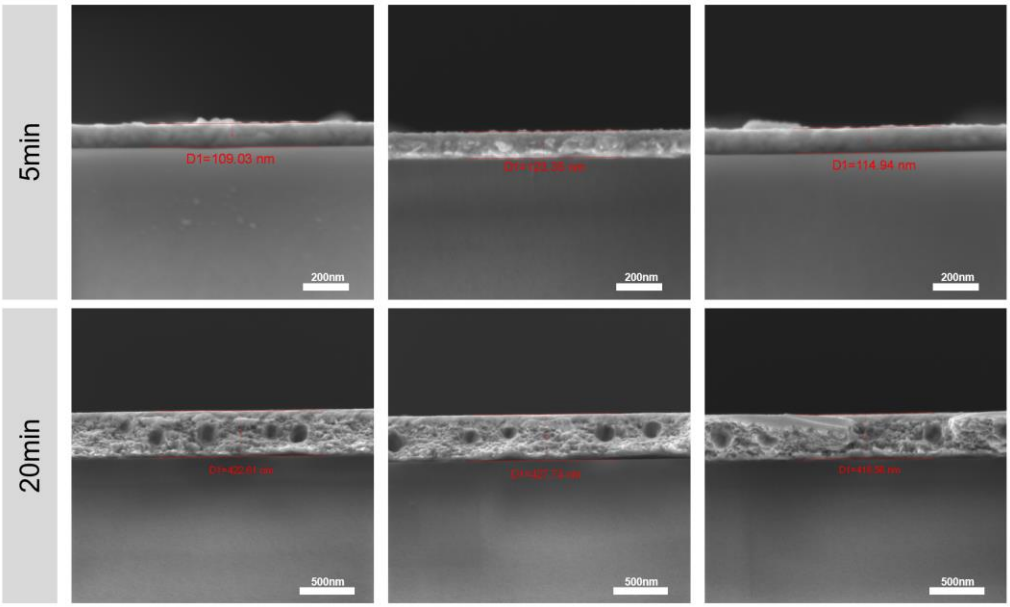

Figure S1. The cross-sectional scanning electron micrographs of Cu film on a glass substrate with different sputtering time under a direct current mode with a power of 50W.

Table S1. Thickness of Cu film with different sputtering time.

Sputtering time (min)	Thickness (nm) obtained from each measurement			
	1	2	3	Average
5	114.94	109.03	123.35	115.77±7.2
20	427.74	422.61	418.58	422.98±4.6

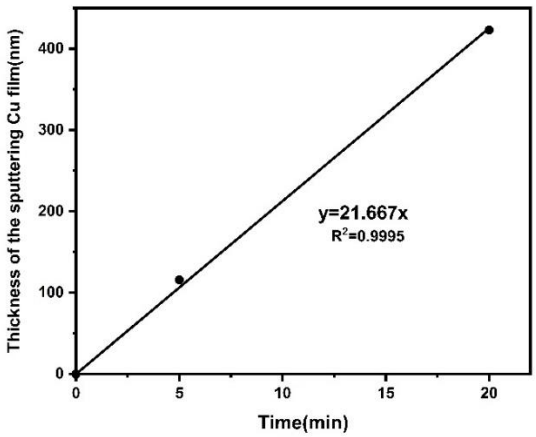

Figure S2. Fitting plot of the thickness of Cu film as a function of sputtering time.

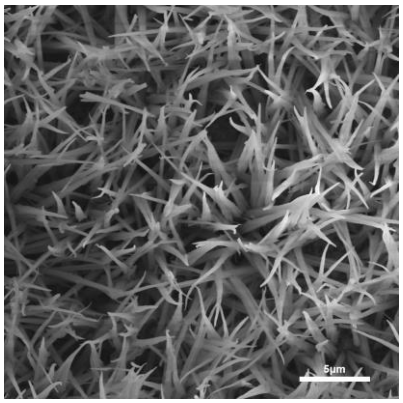

Figure S3. Scanning electron micrograph of CuO NWs/GDL.

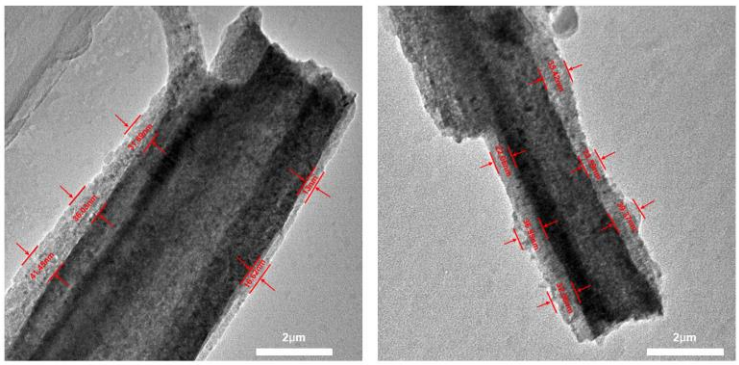

Figure S4. Representative transmission electron micrographs of CuO-In, with the In coating time of 628 s. The thickness of the In layer was measured by Gatan Digital Micrograph software.

Table S2. The thickness of the In layer on the CuO nanowires as determined from Supplementary Figure S4.

The thickness of Indium (nm)											
1	2	3	4	5	6	7	8	9	10	11	Average
41.45	22.06	36.95	32.06	35.42	23.59	39.37	36.03	31.89	16.61	13.00	29.91±9.61

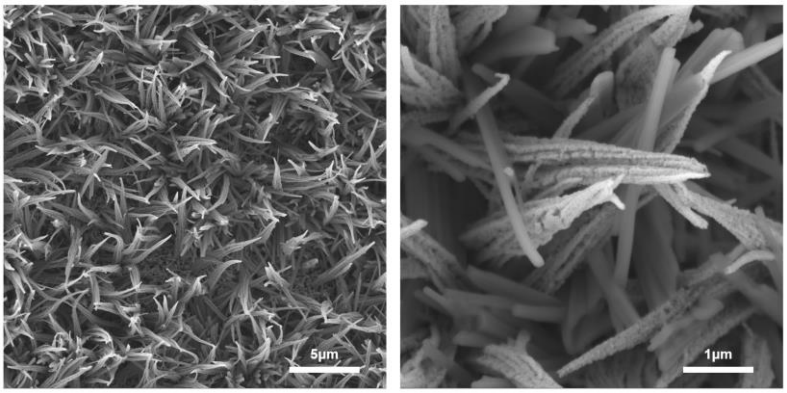

Figure S5. Scanning electron micrographs of Cu/GDE.

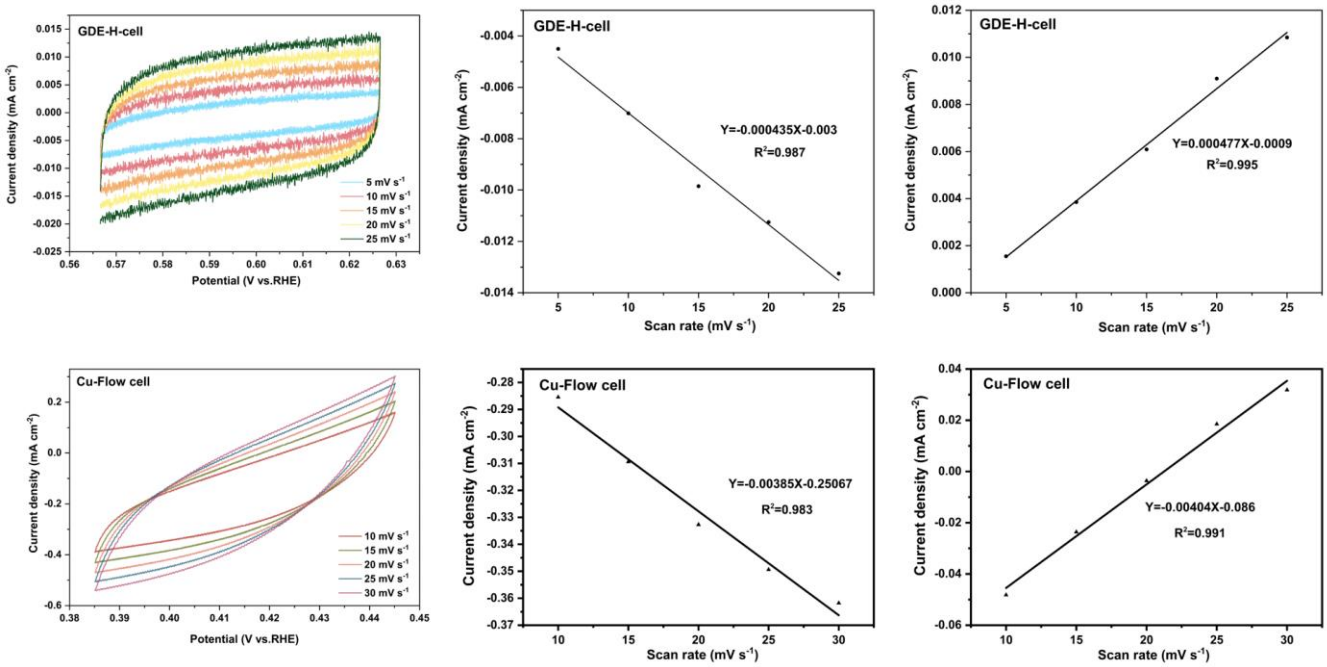

Figure S6. Cyclic voltammograms performed at different scan rates of 5, 10, 15, 20 to 25 mV s^{-1} for GDE and 10, 15, 20, 25 to 30 mV s^{-1} for Cu catalysts and the respective fitting plots of non-faradaic current versus scan rate in Ar-saturated 0.5 M $KHCO_3$.

Table S3. The roughness factors of GDE and Cu catalysts estimated from double layer capacitance.

Catalysts	Double layer capacitance (mF cm^{-2})	Roughness factor
GDE	0.47	16.08
Cu	3.95	136.15

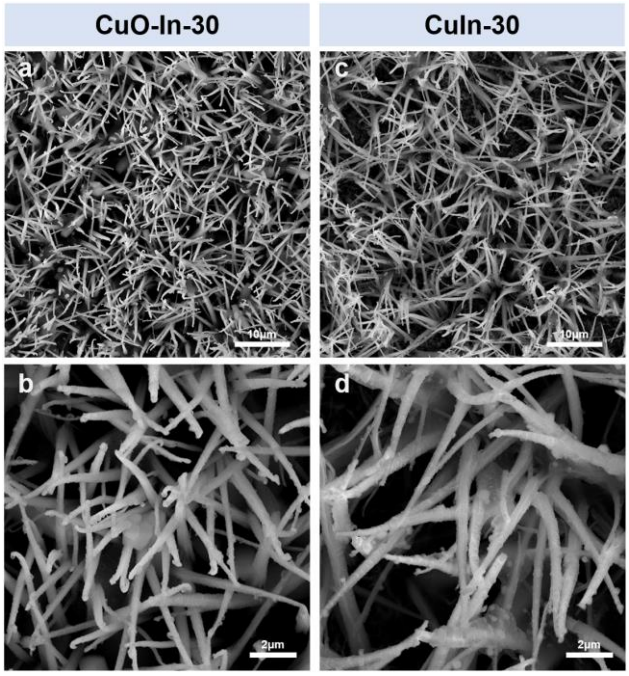

Figure S7. SEM images of CuO-In-30 (a, b) and CuIn-30 (c, d). Scale bars: 10 μm for (a) and (c), 2 μm for (b) and (d).

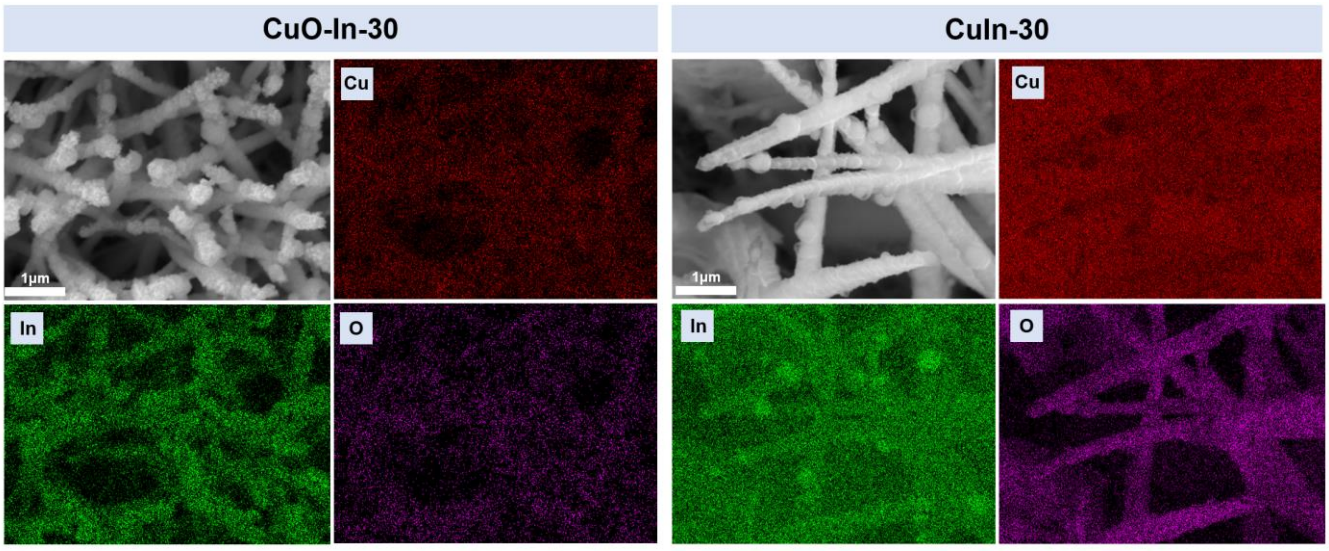

Figure S8. SEM-EDX mapping of CuO-In-30 and CuIn-30.

Table S4. Bulk atomic percentages of different elements in CuO-In-30 and CuIn-30, as analyzed by SEM-EDX.

Sample	C	O	Cu	In	Cu/In
CuO-In-30	12.30	31.49	32.37	23.84	1.36
CuIn-30	10.97	16.14	56.00	16.89	3.32

Table S5. ICP-MS analysis of different element in the electrolyte before and after pre-reduction of CuO-In-30.

Sample	Cu (μg)	In (μg)
Before reduction	0.042	0.001
After reduction	1.925	5.245

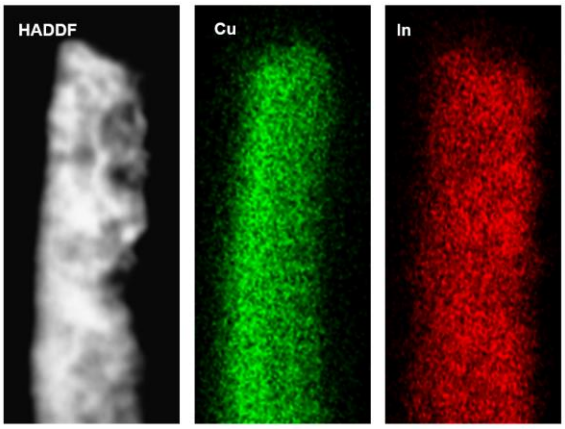

Figure S9. TEM-EDX mapping of CuIn-30 catalyst.

Table S6. Surface atomic percentages of different elements in CuO-In-30 and CuIn-30, as analyzed by XPS.

Sample	Cu	In	Cu/In
CuO-In-30	21	79	0.27
CuIn-30	68	32	2.13

S3. Electrochemical Setup for the Reduction of CO_2 or CO

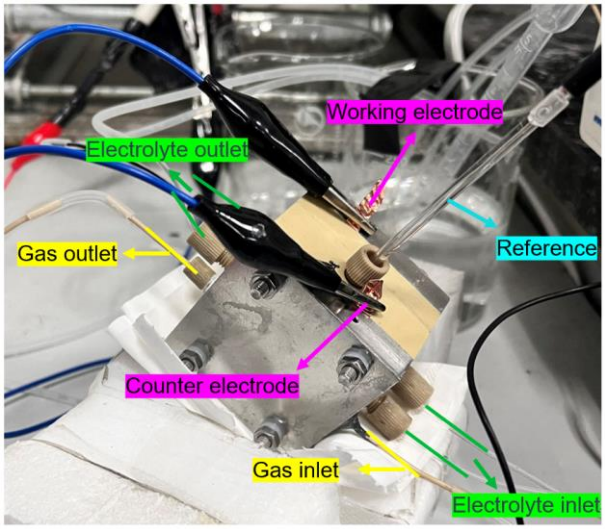

Figure S10. A photograph of the custom-built flow cell used for electrochemical reduction of CO_2 or CO.

Our electrochemical cell is designed based on the structure shown by Kenis and co-workers.[1] The electrochemical cell is composed of four chambers. They are the cathode gas chamber, the cathode electrolyte chamber, the anode electrolyte chamber and the anode gas chamber. The reference electrode is inserted adjacent to the cathode electrolyte chamber. Our anode chamber consists of a gas chamber and a liquid chamber since we employed the gas diffusion electrode for anodic reaction, which is water oxidation to oxygen.

The identification and quantification of gaseous products were done through a gas chromatography (Fuli, GC 9790), equipped with a flame ionization detector (FID) and a thermal conductivity detector (TCD). The signals were calibrated using standard calibration gas (Zhonghao Guangming Chemical Research and Design Institute Co., Ltd.), including known concentration of hydrogen, carbon monoxide, methane, ethylene, and ethane. Carbon dioxide is the balance gas. The calibration plots for the gas products are given in **Figure S11**. The identification and quantification of liquid products were done after electrolysis through a high-performance liquid chromatography (HPLC, Agilent 1260), equipped with a variable wavelength detector (VWD). The signals were calibrated using prepared calibration solutions, with known concentrations of formate, acetate, ethanol and *n*-propanol dissolved in 0.5 M $KHCO_3$. The calibration plots for the liquid products are given in **Figure S12**.

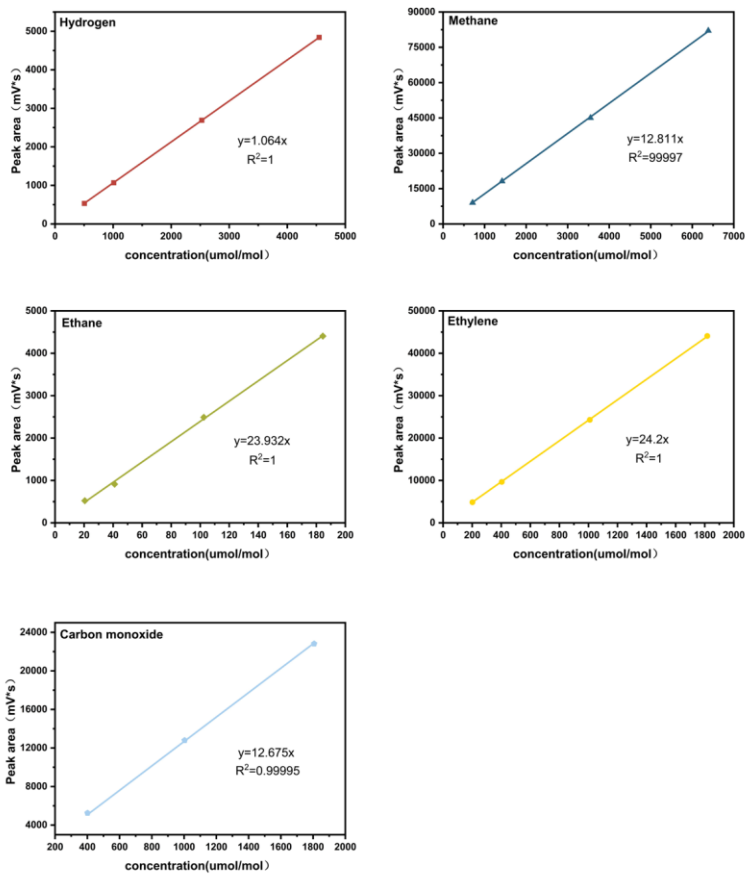

Figure S11. Linear fitting curve for different gaseous products. The absolute peak area in the gas chromatograph is plotted as a function of the concentration of hydrogen, methane, ethane, ethylene and carbon monoxide.

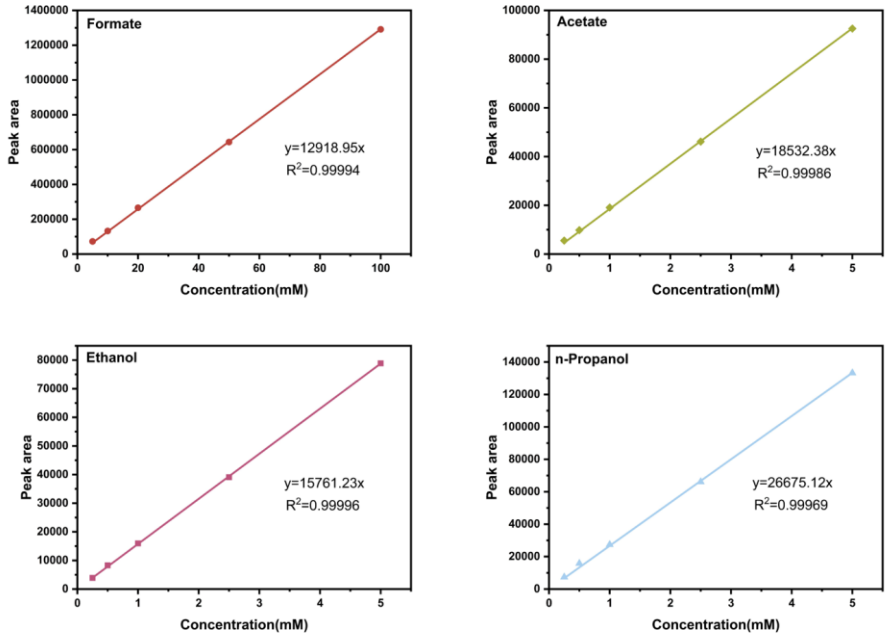

Figure S12. Linear fitting curve for different liquid products. The absolute peak area in the liquid chromatograph is plotted against the concentration of formate, acetate, ethanol and *n*-propanol.

The selectivity of the products is expressed as Faradaic efficiency. The Faradaic efficiency (FE) for product X is defined as:

$$FE(X) = \frac{number\ of\ electrons\ used\ for\ producing\ X\ from\ CO_2}{total\ number\ of\ electrons\ for\ electrolysis} \times 100\% \qquad (1)$$

The amount of gas products (n_x) were calculated via the peak area and the calibration curve (**Figure S11**). The charge Q_x used for producing molecule X is calculated as:

$$Q_x = n_x \times N_x \times F \qquad (2)$$

N_x is the number of electron transfer per product molecule formed from CO_2 or CO. F is Faraday constant (96485.3 C mol^{-1}).

The total charge Q_{total} can be calculated as:

$$Q_{total} = \int_t^{t+t_0} I \times d_t = I_0 \times t_0 = I_0 \times \frac{V}{v} \qquad (3)$$

I_0 is the absolute value of the average current during the injection. V is the volume of sample loop. v is the flow rate of CO_2/CO.

The Faradaic efficiency of gas *x* for this injection is:

$$FE_x = \frac{Q_x}{Q_{total}} \times 100\% = \frac{n_x \times N_x \times F}{I_0 \times \frac{V}{v}} \times 100\% = \frac{n_x \times N_x \times F \times v}{I_0 \times V} \times 100\% \qquad (4)$$

The Faradaic efficiency of liquid product *y* is expressed as:

$$FE_y = \frac{c_y \times V_e \times F}{Q_e} \times 100\% \quad (5)$$

The concentration of product *y* (c_y) is determined via the peak area and the calibration curve (**Figure S12**). V_e is the volume of the electrolyte. Q_e is the total amount of charge throughout the electrolysis.

S4. j-V Curves and Tabulated Faradaic Efficiency for Different Products

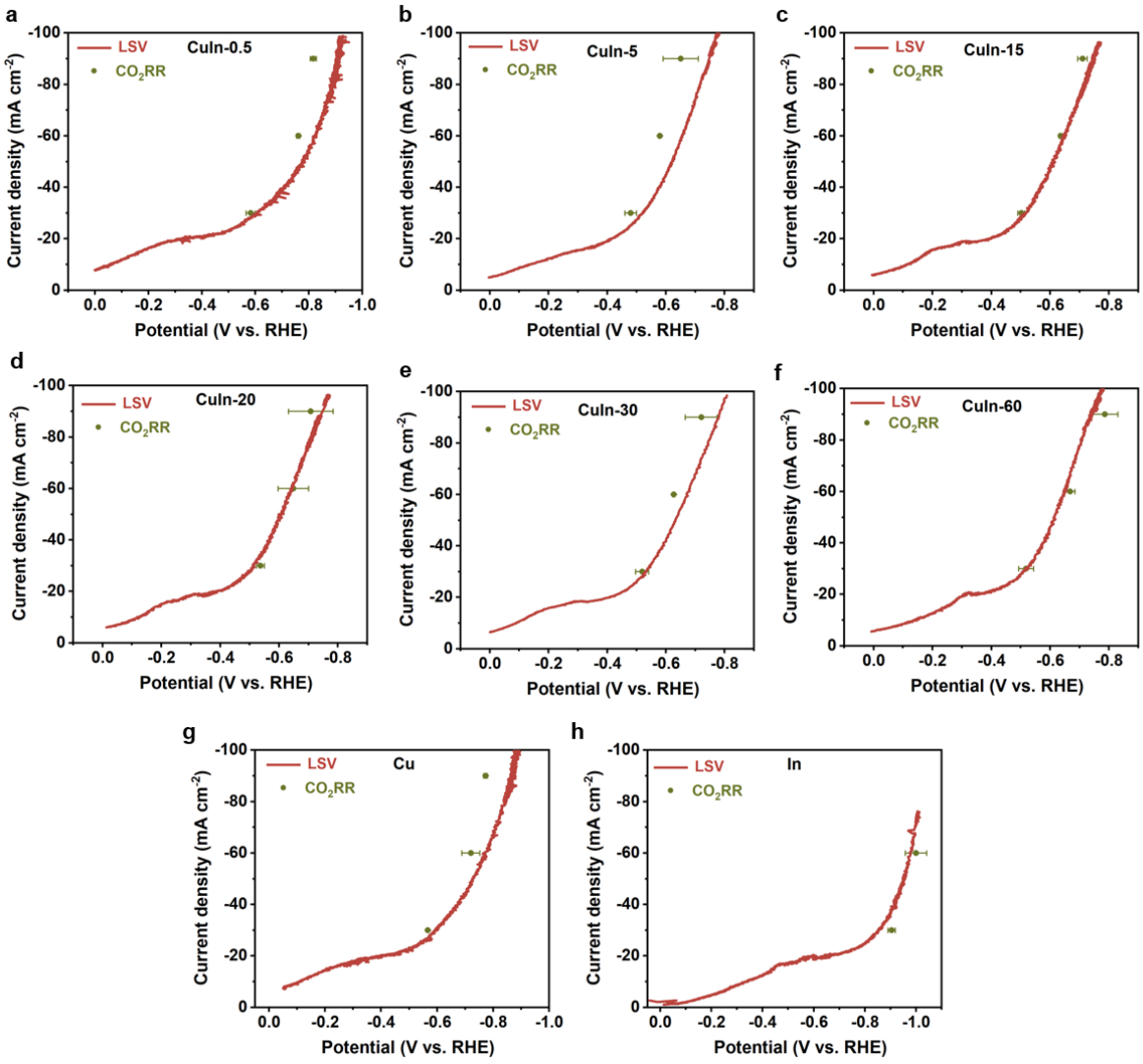

Figure S13. Linear sweep voltammograms of catalysts.

Table S7. Faradaic efficiency of products from CO_2 electroreduction on Cu at different current density. N.D.: Not detectable.

j/mAcm^{-2}	Faraday Efficiency/%								
	CO	**C_2H_4**	**CH_4**	**H_2**	**Formate**	**Acetate**	**Ethanol**	**n-Propanol**	**Total**
-41.6±0.3	23.31%±0.51%	8.41%±0.21%	N.D.	49.61%±0.91%	8.51%±0.11%	N.D.	2.11%±0.21%	N.D.	91.81%±0.61%
-55.0±2.2	16.21%±2.81%	6.11%±4.01%	N.D.	54.81%±10.01%	10.41%±1.21%	N.D.	0.91%±1.31%	N.D.	88.41%±3.11%
-72.2±4.6	19.71%±1.11%	13.71%±4.31%	N.D.	44.61%±7.91%	8.21%±4.11%	N.D.	1.11%±0.81%	N.D.	87.31%±9.61%
-80.6±2.8	21.11%±1.21%	21.01%±0.61%	N.D.	34.61%±0.91%	13.11%±0.21%	N.D.	3.01%±0.11%	N.D.	96.21%±1.41%
-110.0±0.0	19.11%±0.91%	23.71%±2.11%	N.D.	29.71%±2.51%	4.31%±5.51%	1.21%±0.21%	9.81%±1.71%	2.51%±1.31%	90.31%±1.81%
-191.4±0.0	16.01%±0.71%	36.11%±2.61%	1.11%±0.31%	11.71%±1.71%	8.11%±1.21%	1.01%±0.71%	10.11%±3.01%	3.21%±1.11%	87.31%±6.51%
-250.0±0.0	13.71%±0.51%	39.31%±0.81%	1.01%±0.11%	15.71%±0.81%	7.11%±0.71%	2.01%±0.01%	15.91%±0.41%	3.11%±0.61%	97.71%±0.81%

Table S8. Faradaic efficiency of products from CO_2 electroreduction on CuIn-0.5 at different current density. N.D.: Not detectable.

j/mAcm^{-2}	Faraday Efficiency/%							
	CO	**C_2H_4**	**H_2**	**Formate**	**Acetate**	**Ethanol**	**n-Propanol**	**Total**
-40.0	37.11%±3.41%	5.71%±0.21%	29.71%±3.91%	14.21%±2.41%	0.41%±0.41%	7.01%±2.61%	N.D.	94.01%±0.51%
-50.0	25.81%±3.21%	3.91%±1.11%	42.01%±2.31%	15.31%±2.01%	3.81%±1.01%	3.81%±0.71%	N.D.	94.61%±3.91%
-60.0	21.21%±0.41%	6.41%±0.21%	40.21%±1.91%	15.81%±1.11%	3.21%±3.21%	7.11%±2.41%	N.D.	94.01%±2.21%
-70.0	24.81%±0.21%	6.81%±0.21%	37.91%±1.81%	17.91%±0.01%	0.61%±0.91%	5.61%±2.61%	3.91%±0.61%	99.91%±0.81%
-80.0	25.31%±1.11%	11.61%±1.11%	29.41%±0.61%	14.31%±1.31%	1.41%±0.31%	6.01%±0.41%	4.91%±0.81%	92.81%±1.41%

Table S9. Faradaic efficiency of products from CO_2 electroreduction on CuIn-5 at different current density. N.D.: Not detectable.

j/mA cm^{-2}	Faraday Efficiency/%					
	CO	C_2H_4	CH_4	H_2	Formate	Total
-43.6±0.6	71.31%±5.41%	1.81%±1.51%	N.D.	21.81%±4.51%	5.41%±2.91%	100.31%±3.61%
-54.6±1.2	74.41%±3.31%	1.41%±1.21%	N.D.	15.31%±5.71%	3.71%±1.51%	94.91%±5.01%
-60.8±3.0	69.41%±1.41%	3.21%±3.51%	N.D.	16.21%±3.61%	6.01%±4.71%	86.41%±1.61%
-73.9±3.4	69.91%±1.61%	3.81%±0.61%	0.31%±0.11%	15.41%±1.41%	5.71%±0.31%	95.11%±0.61%
-82.1±3.8	68.21%±3.71%	4.61%±1.21%	N.D.	16.01%±4.51%	5.51%±1.81%	97.51%±2.51%

Table S10. Faradaic efficiency of products from CO_2 electroreduction on CuIn-10 at different current density. N.D.: Not detectable.

j/mA cm^{-2}	Faraday Efficiency/%			
	CO	C_2H_4	H_2	Total
-25.1±1.3	57.21%±3.91%	0.81%±0.11%	0.61%±0.81%	58.61%±4.51%
-46.9±4.3	76.21%±5.81%	N.D.	1.41%±1.41%	77.71%±7.21%
-53.7±2.7	82.31%±1.11%	N.D.	0.41%±0.01%	82.71%±1.11%
-60.0±5.6	80.21%±6.61%	N.D.	1.01%±0.01%	81.31%±6.71%
-69.7±3.8	86.01%±7.81%	0.61%±0.61%	1.41%±0.91%	87.91%±8.11%
-81.4±9.6	77.81%±2.21%	N.D.	1.41%±0.31%	79.11%±1.91%

Table S11. Faradaic efficiency of products from CO_2 electroreduction on CuIn-20 at different current density. N.D.: Not detectable.

j/mA cm^{-2}	Faraday Efficiency/%				
	CO	C_2H_4	H_2	Formate	Total
-54.5±0.0	81.61%±1.91%	0.21%±0.31%	0.61%±0.11%	3.51%±0.21%	85.91%±2.11%
-63.8±5.4	82.51%±2.11%	0.41%±0.61%	0.71%±0.31%	2.71%±0.91%	86.41%±2.01%
-68.4±0.5	81.61%±2.11%	N.D.	1.11%±0.61%	3.31%±2.81%	86.01%±5.51%
-71.3±4.6	89.01%±8.41%	N.D.	1.31%±0.41%	3.91%±2.01%	94.21%±6.11%
-81.1±7.0	82.61%±1.31%	N.D.	2.81%±0.61%	6.51%±0.91%	91.81%±1.61%

Table S12. Faradaic efficiency of products from CO_2 electroreduction on CuIn-30 at different current density. N.D.: Not detectable.

j/mAcm^{-2}	Faraday Efficiency/%				
	CO	C_2H_4	H_2	Formate	Total
-40.6±4.9	83.61%±0.21%	N.D.	1.91%±1.51%	2.51%±1.31%	93.11%±3.11%
-49.7±3.5	84.41%±5.41%	0.11%±0.11%	0.71%±0.21%	0.81%±1.11%	83.11%±2.81%
-63.2±1.5	89.91%±5.51%	N.D.	1.31%±0.81%	1.61%±0.61%	92.81%±6.91%
-69.0±0.2	91.21%±2.91%	0.31%±0.21%	1.01%±0.41%	1.71%±1.01%	94.11%±1.41%
-79.5±1.1	87.41%±1.91%	N.D.	1.21%±0.31%	1.81%±0.01%	90.41%±2.21%

Table S13. Faradaic efficiency of products from CO_2 electroreduction on CuIn-60 at different current density. N.D.: Not detectable.

j/mA cm^{-2}	Faraday Efficiency/%								
	CO	**C_2H_4**	**CH_4**	**H_2**	**Formate**	**Acetate**	**Ethanol**	**n-Propanol**	**Total**
-50.0±0.0	62.81%±0.91%	N.D.	N.D.	1.31%±0.11%	17.21%±0.51%	N.D.	N.D.	N.D.	81.41%±0.31%
-60.0±0.0	62.51%±3.61%	N.D.	N.D.	1.91%±0.31%	19.71%±0.81%	N.D.	N.D.	N.D.	84.11%±4.61%
-70.0±0.0	62.71%±1.81%	N.D.	N.D.	1.81%±0.21%	16.51%±3.11%	N.D.	N.D.	N.D.	81.01%±1.11%
-80.0±0.0	63.41%±0.71%	N.D.	N.D.	1.61%±0.11%	21.41%±4.01%	N.D.	N.D.	N.D.	86.41%±3.31%
-90.0±0.0	60.41%±0.31%	N.D.	N.D.	1.81%±0.11%	19.11%±2.61%	N.D.	N.D.	N.D.	81.31%±2.91%
-100.0±0.0	62.41%±3.81%	N.D.	N.D.	1.81%±0.01%	15.71%±0.91%	N.D.	N.D.	N.D.	79.91%±2.91%
-150.0±0.0	28.91%±3.41%	7.81%±1.51%	0.04%±0.03%	8.61%±1.71%	20.11%±1.91%	0.91%±0.11%	10.01%±3.11%	4.71%±1.51%	81.11%±6.21%
-200.0±0.0	29.21%±4.61%	19.91%±5.91%	0.13%±0.02%	7.91%±1.01%	18.71%±1.91%	1.11%±0.11%	13.11%±0.91%	6.41%±0.81%	96.51%±0.11%

Table S14. Faradaic efficiency of products from CO_2 electroreduction on In at different current density.

j/mA cm^{-2}	Faraday Efficiency/%			
	CO	**H_2**	**Formate**	**Total**
-42.3±2.7	3.21%±0.01%	2.31%±0.71%	45.31%±8.41%	50.81%±7.71%
-53.0±1.3	2.21%±0.21%	2.61%±1.61%	51.41%±1.61%	56.21%±3.01%
-64.4±0.6	2.61%±0.11%	1.81%±0.21%	53.01%±13.11%	57.41%±12.71%
-80.5±1.5	2.21%±0.31%	5.31%±0.31%	54.21%±8.61%	61.61%±9.11%
-105.6±7.1	2.01%±0.11%	4.71%±0.61%	71.31%±0.81%	78.01%±1.41%

Table S15. Faradaic efficiency of products from CO_2 electroreduction on CuIn-X catalysts at about -140 mA cm^{-2}. N.D.: Not detectable.

Catalyst	Faraday Efficiency/%								
	CO	C_2H_4	CH_4	H_2	Formate	Acetate	Ethanol	n-Propanol	Total
CuIn-15	26.21%±0.31%	16.31%±0.61%	N.D.	22.21%±0.31%	5.01%±0.11%	1.31%±0.11%	9.01%±0.21%	2.11%±0.21%	82.11%±0.11%
CuIn-20	37.11%±1.41%	9.91%±0.71%	0.11%±0.01%	14.91%±5.31%	2.81%±1.21%	0.91%±0.11%	8.81%±0.41%	1.21%±0.11%	75.61%±8.31%
CuIn-30	66.41%±1.51%	N.D.	N.D.	6.41%±1.21%	12.01%±4.01%	1.31%±0.31%	4.31%±2.41%	0.51%±0.21%	90.91%±6.61%

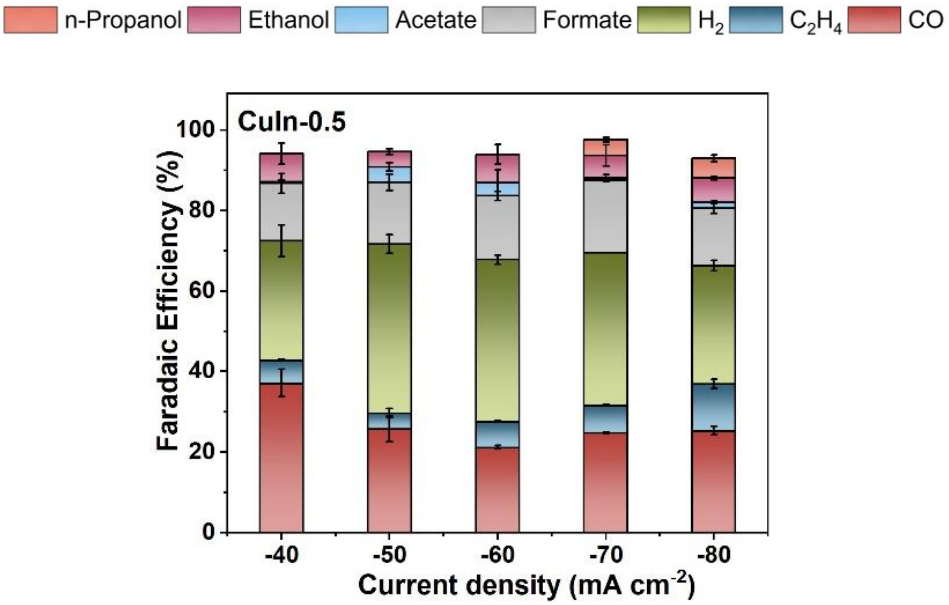

Figure S14. Faradaic efficiency of different products on CuIn-0.5.

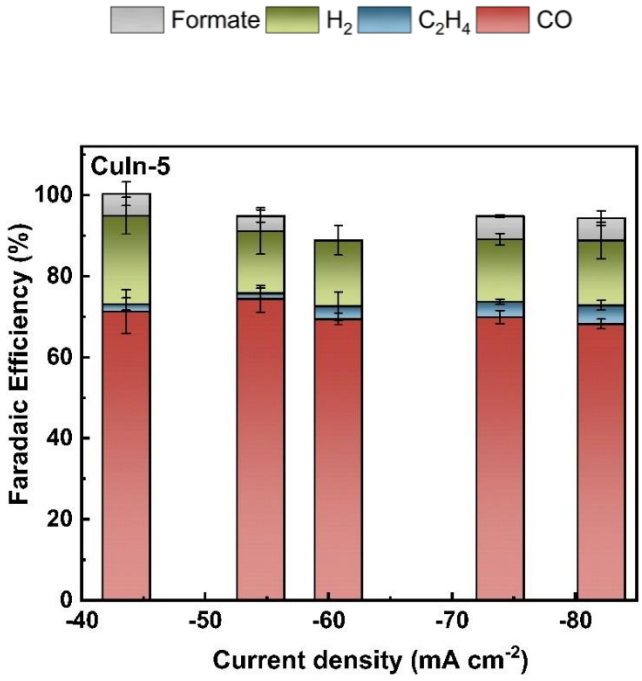

Figure S15. Faradaic efficiency of different products on CuIn-5.

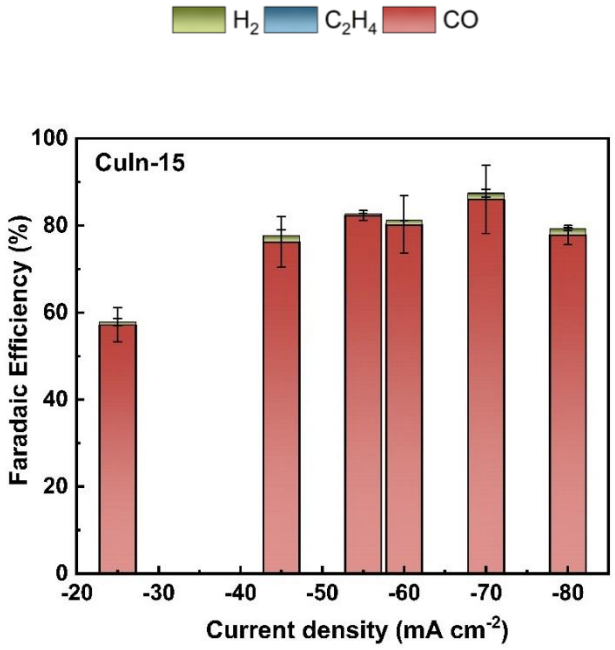

Figure S16. Faradaic efficiency of different products on CuIn-15.

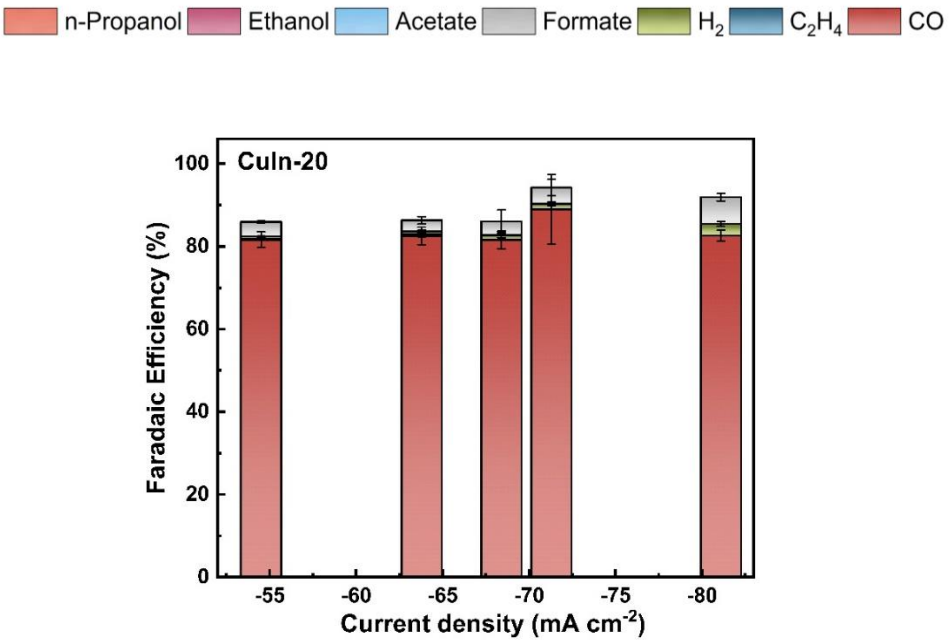

Figure S17. Faradaic efficiency of different products on CuIn-20.

S5. A Summary of Efficient Catalysts for CO_2 Reduction to CO.

Table S16. Comparison of CO_2RR to CO performances for Cu-based catalysts.

Catalyst	Catholyte	Electrolyzer	Current density (mA cm^{-2})	Faraday efficiency	Ref.
CuIn-30	0.5M $KHCO_3$	Flow-Cell	-70.0	93.0%	This work
Cu-S-Ni/SNC	0.1M $KHCO_3$	H-Cell	-24.5	98.1%	Sun et al.[2]
Cu/In_2O_3	0.1M $KHCO_3$	H-Cell	-3.0 [a]	78.0%	Du et al.[3]
Sb_1Cu-5	0.5M $KHCO_3$	Flow Cell	-150.0	95.0%	Li et al.[4]
Cu-SnO_2	0.5M $KHCO_3$	Flow Cell	-50.0	98.0%	Gao et al.[5]
$CuIn_{20}$	0.1M $KHCO_3$	H-Cell	-4.2	93.0%	Luo et al.[6]
$Cu_{11}In_9$	0.5M $KHCO_3$	H-Cell	-3.0 [a]	90.0%	He et al.[7]

a: This value is estimated from the graph in the corresponding article.

Table S17. Comparison of CO_2RR to CO performances for non-Cu-based catalysts.

Catalyst	Catholyte	Electrolyzer	Current density (mA cm^{-2})	Faraday efficiency	Ref.
CuIn-30	0.5M $KHCO_3$	Flow-Cell	-70.0	93.0%	This work
Zn_1Mn_1-SNC	0.1M $KHCO_3$	H-Cell	-10.2	97.0%	Pei et al.[8]
Ni-N-C	0.5M $KHCO_3$	H Cell	-37.6	98.5%	Zhou et al.[9]
FeN/Fe_3N	0.5M $KHCO_3$	H-Cell	-4.0 [a]	98.0%	Yin et al.[10]
NC@Ni/C	0.5M $KHCO_3$	H-Cell	-90.0 [a]	97.0%	Lu et al.[11]
$Au_{22}H_3$	0.5M $KHCO_3$	H-Cell	-7.0 [a]	92.7%	Gao et al.[12]
Au nanoparticles	1 M Cs_2SO_4	Flow Cell	-200.0	80-90%	Monteiro et al.[13]
Ni-N-hCNCs	0.5M $KHCO_3$	H-Cell	-10.0 [a]	87.0%	Chen et al.[14]
$CoPc_2$	1 M KOH	Flow Cell	-111.6	95.0%	Wang et al.[15]
Ag100 dendrite	0.5M $KHCO_3$	H-Cell	-	64.6%	Choi et al.[16]
3D-Ag	0.1M $KHCO_3$	H-Cell	-6.4	88.8%	Qiu et al.[17]
CD-AgHPE	3 M KCl and H_2SO_4	Flow Cell	-4300.0	95.0%	Li et al.[18]
Ni–NC–NS	0.5M $KHCO_3$	H-Cell	-26.8	100.0%	Cho et al.[19]
NiPc-OMe MDE	0.5 M K_2SO_4 and H_2SO_4	Flow Cell	-400.0	>99%	Jiang et al.[20]

a: This value is estimated from the graph in the corresponding article.

S6. Oxidation of Formate at Pt Electrode.

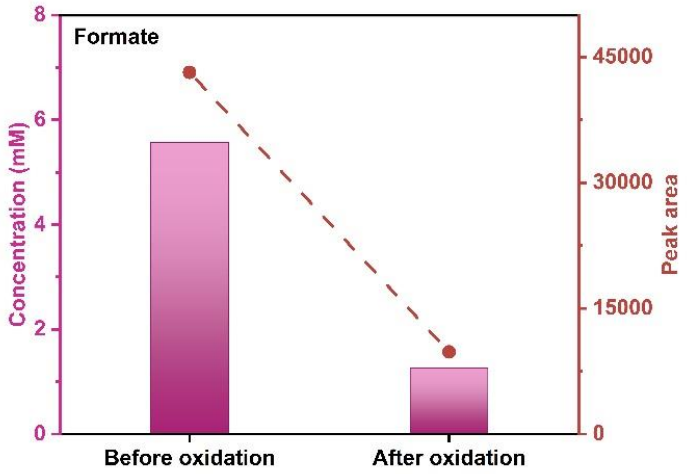

Figure S18. The concentration of formate and the peak area in the liquid chromatography for formate for the electrolyte before oxidation process and after oxidation process. The oxidation was carried out in 0.5 M $KHCO_3$ at a constant geometric current density of 50 mA cm^{-2} for 1h through the utilization of a two-electrode configuration with Pt and carbon rod as the working electrode and counter electrode, respectively.

S7. Materials Characterizations after Long-term Electrolysis

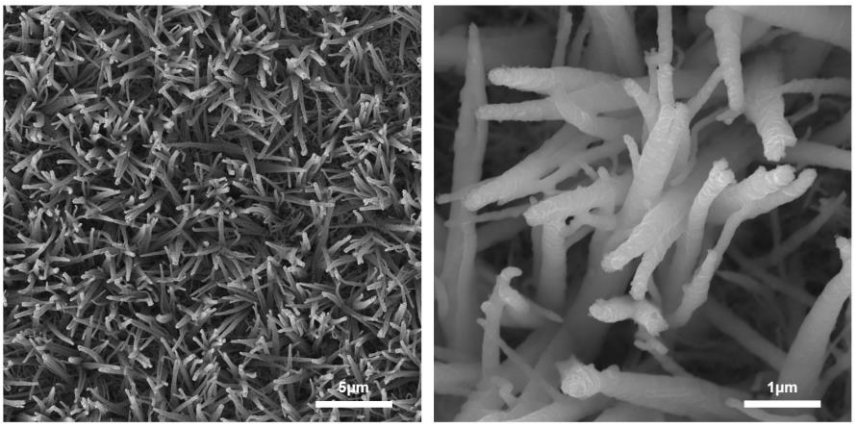

Figure S19. SEM images of CuIn-30 after stability test.

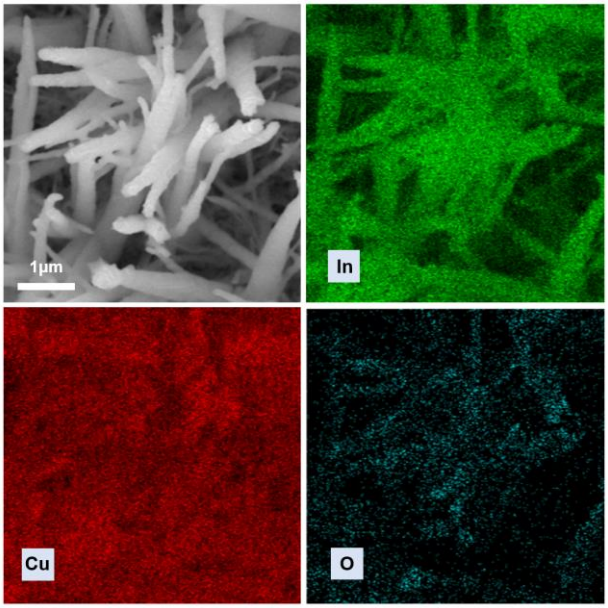

Figure S20. SEM-EDX mapping of CuIn-30 after stability test.

Table S18. Bulk atomic percentages of different elements in CuIn-30 before and after stability test, as analyzed by SEM-EDX.

Sample	C	O	Cu	In	Cu/In
CuIn-30 (before stability test)	10.97	16.14	56.00	16.89	3.32
CuIn-30 (after stability test)	7.71	1.82	62.99	27.48	2.29

Table S19. ICP-MS analysis of different element in the electrolyte before and after long stability test.

Sample	Cu (μg)	In (μg)
CuIn-30 (before stability test)	0.008	0.133
CuIn-30 (after stability test)	4.615	2.017

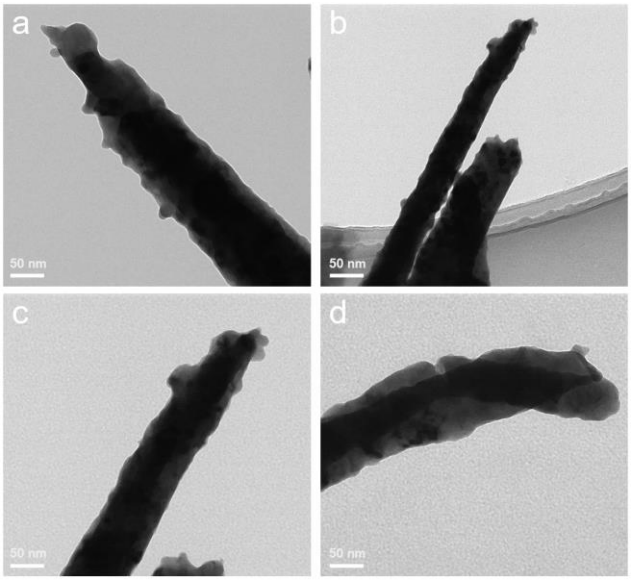

Figure S21. Representative TEM images of CuIn-30 after stability test.

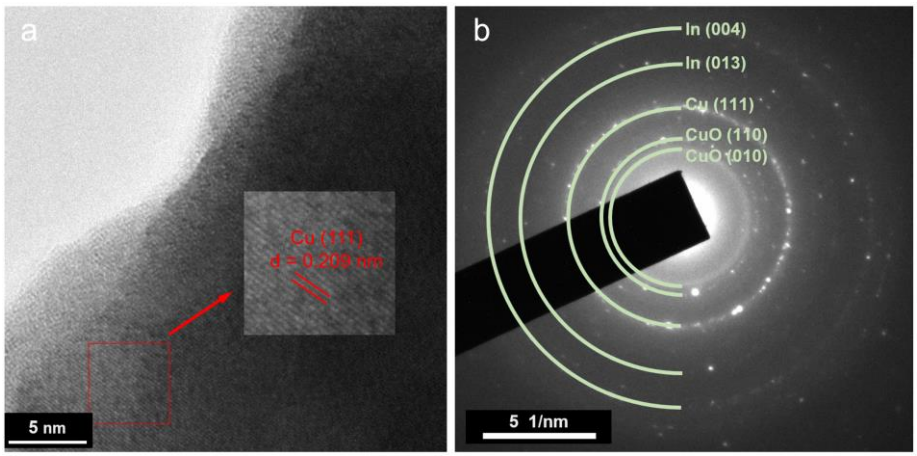

Figure S22. Structural characterizations of CuIn-30 catalysts after stability test. (a) Representative HRTEM images and (b) SAED pattern of CuIn-30 after stability test. Manually drawn arcs mark the diffraction rings for d-spacing calibration.

S8. Electrochemical *OH Adsorption

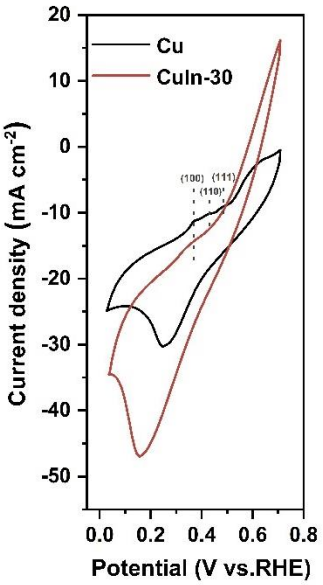

Figure S23. *OH adsorption measurements on Cu and CuIn-30 catalysts. Cyclic voltammograms recorded on Cu and CuIn-30 in 1.0 M KOH aqueous solution. The curves were recorded at a scan rate of 100 mV s^{-1}.

S9. Temperature-programmed Desorption

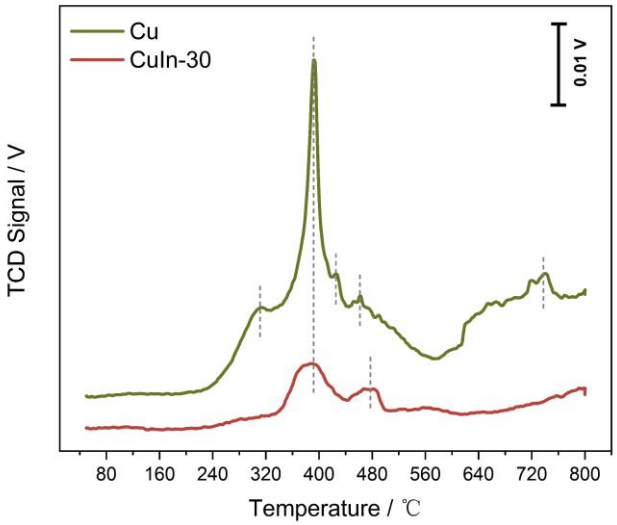

Figure S24. Temperature-programmed desorption (TPD) spectra of Cu and CuIn-30 catalysts.

S10. Electrochemical Reduction of CO on Cu and Cu-In Catalysts

Table S20. Faradaic efficiency of products from CO electroreduction on Cu at different current density. N.D.: Not detectable.

J/mA cm^{-2}	Faraday Efficiency/%							
	C_2H_4	CH_4	H_2	Formate	Acetate	Ethanol	n-Propanol	Total
-34.1±1.1	21.41%±0.61%	0.11%±0.21%	37.41%±2.41%	0.11%±0.21%	1.11%±0.21%	11.31%±6.31%	7.01%±1.91%	78.51%±11.01%
-43.2±1.9	25.71%±1.01%	N.D.	39.81%±3.31%	0.31%±0.11%	1.01%±0.61%	10.91%±5.01%	7.31%±5.11%	85.01%±13.21%
-53.5±2.8	22.61%±0.41%	N.D.	30.71%±11.51%	N.D.	1.51%±0.51%	7.61%±1.91%	7.81%±0.41%	70.11%±14.71%
-61.7±0.2	25.41%±1.11%	0.11%±0.21%	46.51%±0.21%	0.01%±0.11%	5.61%±3.11%	5.21%±0.91%	5.01%±2.81%	87.91%±0.11%
-77.4±1.9	26.01%±2.61%	N.D.	40.51%±9.81%	N.D.	1.11%±0.81%	10.31%±0.61%	7.31%±3.11%	85.31%±2.71%
-93.9±2.1	35.11%±10.01%	N.D.	45.71%±2.71%	0.01%±0.11%	2.01%±0.01%	10.11%±0.21%	5.71%±1.51%	98.71%±6.11%

Table S21. Faradaic efficiency of products from CO electroreduction on CuIn-30 at different current density. N.D.: Not detectable.

J/mA cm^{-2}	Faraday Efficiency/%							
	C_2H_4	CH_4	H_2	Formate	Acetate	Ethanol	n-Propanol	Total
-40.0±0.0	3.91%±0.91%	14.51%±2.01%	40.71%±1.11%	2.31%±1.21%	8.11%±1.51%	7.51%±2.01%	3.01%±0.91%	79.91%±1.31%
-52.7±2.6	7.41%±1.81%	8.91%±4.91%	32.61%±3.21%	N.D.	8.61%±2.81%	14.81%±10.11%	3.91%±0.61%	76.21%±7.21%
-57.7±0.6	9.31%±8.11%	5.61%±4.01%	43.71%±7.71%	2.61%±3.51%	4.81%±2.41%	7.91%±2.81%	2.81%±0.51%	76.61%±7.21%
-77.3±2.6	15.41%±5.31%	7.71%±4.51%	38.41%±5.11%	0.71%±0.71%	8.91%±2.91%	14.21%±5.31%	5.51%±4.31%	90.71%±16.21%
-95.0±0.0	32.61%±2.71%	6.51%±0.21%	17.71%±1.51%	N.D.	15.41%±0.81%	17.21%±0.41%	5.21%±2.41%	94.51%±0.21%

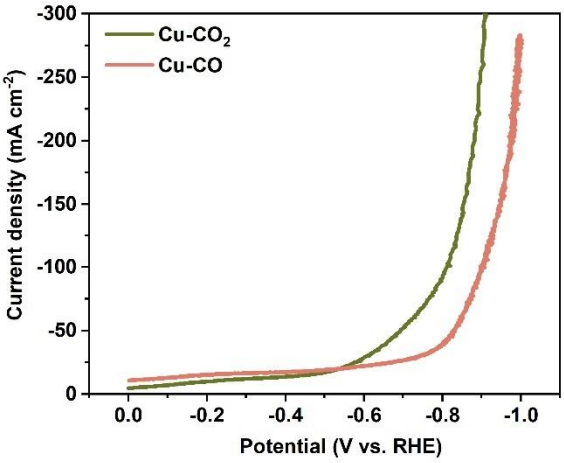

Figure S25. Linear sweep voltammograms of Cu catalyst under the flow of CO_2 or CO.

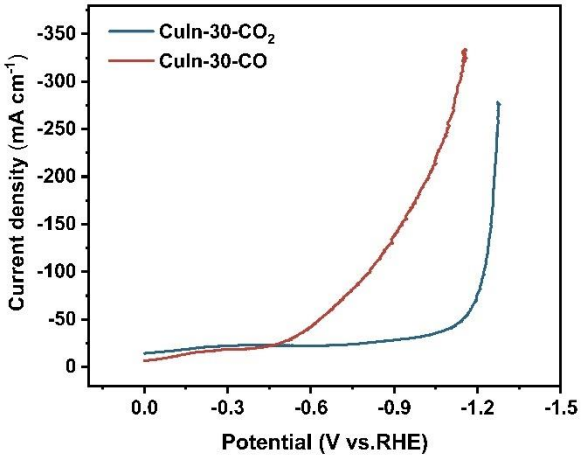

Figure S26. Linear sweep voltammograms of CuIn-30 catalyst under the flow of CO_2 or CO.

S11. *In situ* Raman Setup

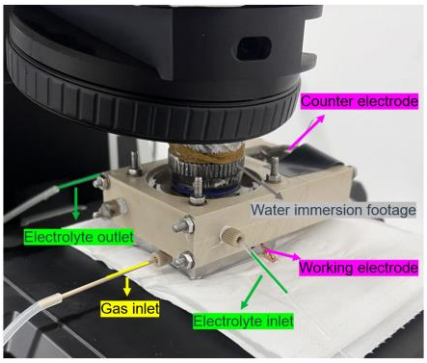

Figure S27. A photograph of the spectro-electrochemical flow cell for acquiring Raman spectra.

S12. DFT Calculation

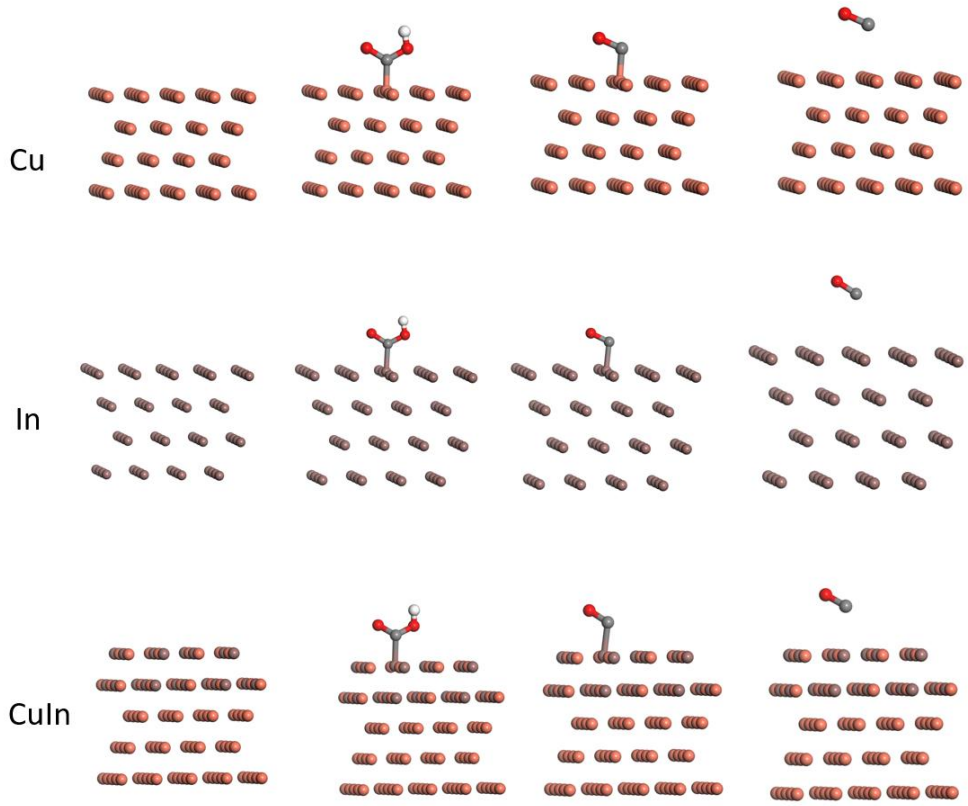

Figure S28. DFT-optimized geometries for each reaction step towards CO on Cu, In and CuIn.

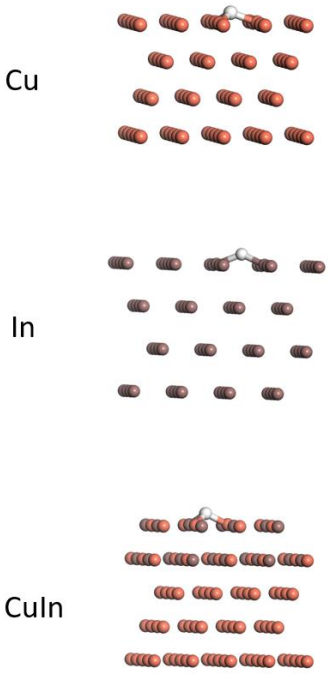

Figure S29. DFT-optimized geometries for each reaction step towards H_2 on Cu, In and CuIn.

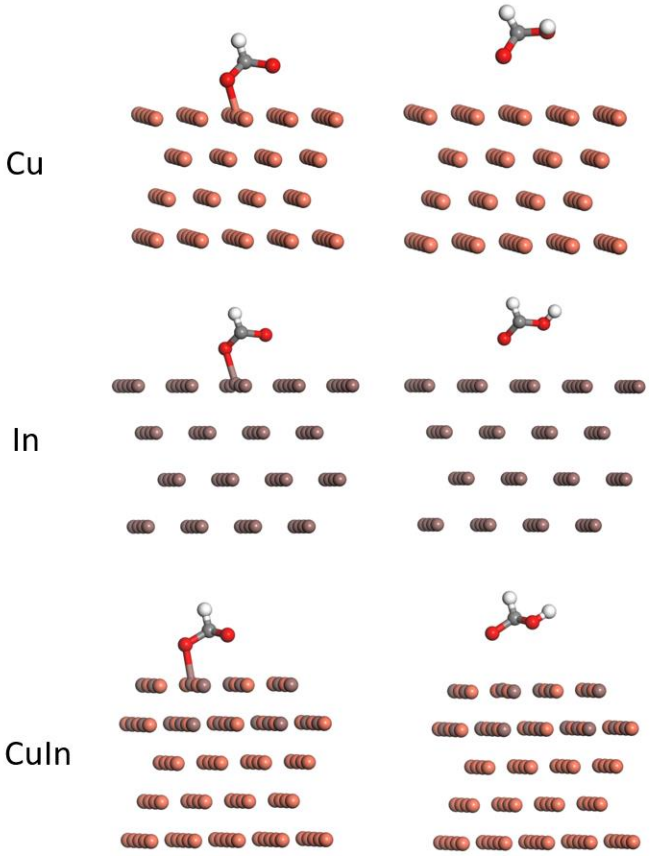

Figure S30. DFT-optimized geometries for each reaction step towards HCOOH on Cu, In and CuIn.

S13. Solar-driven CO_2 Reduction

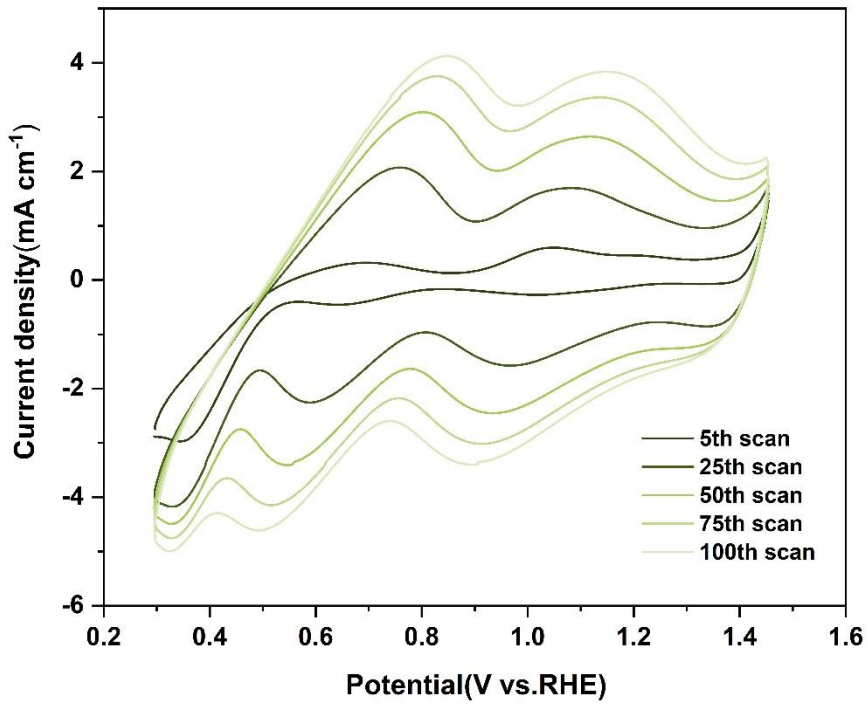

Figure S31. Cyclic voltammograms of the electrodeposition of IrO_x on GDE. Total number of cycles is 100, and the curves for cycle number 5, 25, 50, 75, and 100 are shown.

Calculation of solar-to-fuel (STF) conversion efficiency

For the CO_2 reduction system, the solar to electricity (STE) conversion efficiency can be calculated:

$$\eta_{STE} = \frac{electrtrical\ power\ output}{solar\ illumination\ input} = \frac{j_{op}V_{op}}{P_s}$$

The electricity to fuel (ETF) conversion efficiency can be calculated:

$$\eta_{ETF} = \frac{fuel\ power\ output}{electrtrical\ power\ input} = \frac{j_{op}E_{fuel}FE_{fuel}}{j_{op}V_{op}}$$

Where j_{op} and V_{op} are the operating current and voltage of the combined system, Ps is the solar illumination input power, E_{fuel} is the thermodynamic equilibrium potential between the two half-reactions under standard condition and FE_{fuel} is the faradaic efficiency of the product.

The STF conversion efficiency can be determined directly by the multiplier of STE and ETF :

$$\eta_{STF} = \eta_{STE} \times \eta_{ETF} = \frac{j_{op}V_{op}}{P_s} \times \frac{j_{op}E_{fuel}FE_{fuel}}{j_{op}V_{op}} = \frac{j_{op}E_{fuel}FE_{fuel}}{P_s}$$

For example, calculating the conversion efficiency of solar to CO, The operating current density (the electrolysis current is normalized against the effective illuminated area of the solar cell) of the solar driven CO_2 reduction system is 11.09 mA cm^{-2}. The faradaic efficiency for CO formation was 69.51%. The equilibrium cell potential for ethylene formation is 1.34 V. The solar-to-CO conversion efficiency is calculated as:

$$\eta_{solar\ to\ CO} = \frac{j_{op}E_{fuel}FE_{fuel}}{P_s} = \frac{11.09mA\ cm^{-2} \times 1.34V \times 69.51\%}{100\ mW\ cm^{-2}} = 10.33\%$$

Table S22. Faradaic efficiency and solar-to-fuel efficiency from solar-driven system on CuIn-90 over 105 minutes electrolysis.

Time/min	J/mAcm^{-2}	Faraday Efficiency/%		Solar-to-CO efficiency (%)	Solar-to-H_2 efficiency (%)
		CO	H_2		
5.0	-11.09	69.51%	3.88%	10.33%	0.10%
19.2	-10.87	69.25%	3.70%	10.09%	0.10%
33.4	-10.86	67.92%	3.69%	9.88%	0.10%
47.6	-10.54	64.43%	2.99%	9.10%	0.08%
61.8	-10.43	63.86%	3.44%	8.93%	0.09%
76.0	-10.37	62.25%	1.64%	8.65%	0.04%
90.2	-10.30	62.07%	2.29%	8.57%	0.06%
104.4	-10.24	62.10%	3.22%	8.52%	0.08%
Average	-10.59	65.17%	3.11%	9.26%	0.08%

Table S23. A summary of solar-driven (PV-EC) CO_2 reduction systems.

Cathode	Anode	Catholyte	J_{op} (mA cm^{-2})	Major product/FE	Solar-to-major product	Ref.
CuIn-90	IrO_x	KOH	-11.09	CO/69.5%	10.33%	This work
HRS-Cu	Ni foam	KOH	-41.3	C_{2+}/72%	~6.0%	Gong et al.[21]
Au	IrO_2	$NaHCO_3$	-5.8	CO/85%	6.50%	Schreier et al.[22]
CuO-SnO_2 ALD/GDE	IrO_2	KOH	-14.83	CO/~100%	19.70%	Gao et al.[23]
CuO_2/Ag	IrO_2	$KHCO_3$	-6.7	C_2H_4	4.20%	Gao et al.[24]
Cu/GDE	Se (NiCo)Sx/$(OH)_x$	KOH	-52.4	C_2H_4/C_2H_5OH	3.90%	Gong et al.[25]
Cu_2O	IrO_x	$KHCO_3$	-20	C_2H_4/32%	1.50%	Ren et al.[26]
Au_{25}/GDE	NiFe	KOH	-14.1	CO/~100%	~18%	Kim et al.[27]
Ag/GDE	Ni foam	KOH	-14.4	CO/99%	19.10%	Cheng et al.[28]
CuO-SnO_2 ALD	CuO-SnO_2 ALD	$CsHCO_3$	-11.6	CO/81%	13.40%	Schreier et al.[29]

S14. Supporting References

1. S. Ma, M. Sadakiyo, R. Luo, M. Heima, M. Yamauchi and P. J. A. Kenis, One-step electrosynthesis of ethylene and ethanol from CO_2 in an alkaline electrolyzer, *J. Power Sources*, 2016, **301**, 219-228.
2. Z. Sun, C. Li, Z. Wei, F. Zhang, Z. Deng, K. Zhou, Y. Wang, J. Guo, J. Yang, Z. Xiang, P. Ma, H. Zhai, S. Li and W. Chen, Sulfur-Bridged Asymmetric CuNi Bimetallic Atom Sites for CO_2 Reduction with High Efficiency, *Adv. Mater.*, 2024, **36**, 0935-9648.
3. X. Du, H. Fu, B. Gao, C. Xiao, S. Ding, D. Qian, Z. Song and K. T. Nam, Tuning the selectivity of CO_2 electroreduction on Cu/In_2O_3 heterogeneous interface, *Nano Energy*, 2024, **120**.
4. J. Li, H. Zeng, X. Dong, Y. Ding, S. Hu, R. Zhang, Y. Dai, P. Cui, Z. Xiao, D. Zhao, L. Zhou, T. Zheng, J. Xiao, J. Zeng and C. Xia, Selective CO_2 electrolysis to CO using isolated antimony alloyed copper, *Nat. Commun.*, 2023, **14**.
5. J. Gao, J. Li, Y. H. Liu, M. Xia, Y. Z. Finfrock, S. M. Zakeeruddin, D. Ren and M. Grätzel, Solar reduction of carbon dioxide on copper-tin electrocatalysts with energy conversion efficiency near 20%, *Nat. Commun.*, 2022, **13**.
6. W. Luo, W. Xie, R. Mutschler, E. Oveisi, G. L. De Gregorio, R. Buonsanti and A. Zuttel, Selective and Stable Electroreduction of CO_2 to CO at the Copper/Indium Interface, *ACS Catal.*, 2018, **8**, 6571-6581.
7. J. He, K. E. Dettelbach, D. A. Salvatore, T. Li and C. P. Berlinguette, High-Throughput Synthesis of Mixed-Metal Electrocatalysts for CO_2 Reduction, *Angew. Chem. Int. Ed.*, 2017, **56**, 6068-6072.
8. J. Pei, L. Yang, J. Lin, Z. Zhang, Z. Sun, D. Wang and W. Chen, Integrating Host Design and Tailored Electronic Effects of Yolk-Shell Zn-Mn Diatomic Sites for Efficient CO_2 Electroreduction, *Angew. Chem. Int. Ed.*, 2024, **63**.
9. Y. Zhou, Q. Zhou, H. Liu, W. Xu, Z. Wang, S. Qiao, H. Ding, D. Chen, J. Zhu, Z. Qi, X. Wu, Q. He and L. Song, Asymmetric dinitrogen-coordinated nickel single-atomic sites for efficient CO_2 electroreduction, *Nat. Commun.*, 2023, **14**.
10. J. Yin, J. Jin, Z. Yin, L. Zhu, X. Du, Y. Peng, P. Xi, C.-H. Yan and S. Sun, The built-in electric field across FeN/Fe_3N interface for efficient electrochemical reduction of CO_2 to CO, *Nat. Commun.*, 2023, **14**.
11. Q. Lu, C. Chen, Q. Di, W. Liu, X. Sun, Y. Tuo, Y. Zhou, Y. Pan, X. Feng, L. Li, D. Chen and J. Zhang, Dual Role of Pyridinic-N Doping in Carbon-Coated Ni Nanoparticles for Highly Efficient Electrochemical CO_2 Reduction to CO over a Wide Potential Range, *ACS Catal.*, 2022, **12**, 1364-1374.
12. Z.-H. Gao, K. Wei, T. Wu, J. Dong, D.-E. Jiang, S. Sun and L.-S. Wang, A Heteroleptic Gold Hydride Nanocluster for Efficient and Selective Electrocatalytic Reduction of CO_2 to CO, *J. Am. Chem. Soc.*, 2022, **144**, 5258-5262.

13. M. C. O. Monteiro, M. F. Philips, K. J. P. Schouten and M. T. M. Koper, Efficiency and selectivity of CO_2 reduction to CO on gold gas diffusion electrodes in acidic media, *Nat. Commun.*, 2021, **12**.

14. Y. Chen, Y. Yao, Y. Xia, K. Mao, G. Tang, Q. Wu, L. Yang, X. Wang, X. Sun and Z. Hu, Advanced Ni-N_x-C single-site catalysts for CO_2 electroreduction to CO based on hierarchical carbon nanocages and S-doping, *Nano Res.*, 2020, **13**, 2777-2783.

15. M. Wang, K. Torbensen, D. Salvatore, S. Ren, D. Joulie, F. Dumoulin, D. Mendoza, B. Lassalle-Kaiser, U. Isci, C. P. Berlinguette and M. Robert, CO_2 electrochemical catalytic reduction with a highly active cobalt phthalocyanine, *Nat. Commun.*, 2019, **10**.

16. J. Choi, M. J. Kim, S. H. Ahn, I. Choi, J. H. Jang, Y. S. Ham, J. J. Kim and S.-K. Kim, Electrochemical CO_2 reduction to CO on dendritic Ag–Cu electrocatalysts prepared by electrodeposition, *Chem. Eng. J.*, 2016, **299**, 37-44.

17. Q. Jianping, T. Juntao, S. Jie, W. Cuiwei, Q. Mengqian, H. Zhiqiao, C. Jianmeng and S. Song, Preparation of a silver electrode with a three-dimensional surface and its performance in the electrochemical reduction of carbon dioxide, *Electrochim. Acta*, 2016, **203**, 99-108.

18. S. Li, X. Dong, G. Wu, Y. Song, J. Mao, A. Chen, C. Zhu, G. Li, Y. Wei, X. Liu, J. Wang, W. Chen and W. Wei, Ampere-level CO_2 electroreduction with single-pass conversion exceeding 85% in acid over silver penetration electrodes, *Nat. Commun.*, 2024, **15**, 6101.

19. J. H. Cho, J. Ma, C. Lee, J. W. Lim, Y. Kim, H. Y. Jang, J. Kim, M.-g. Seo, Y. Choi, Y. J. Jang, S. H. Ahn, H. W. Jang, S. Back, J.-L. Lee and S. Y. Kim, Crystallographically vacancy-induced MOF nanosheet as rational single-atom support for accelerating CO_2 electroreduction to CO, *Carbon Energy*, 2024, **6**, 2637-9368.

20. Z. Jiang, Z. Zhang, H. Li, Y. Tang, Y. Yuan, J. Zao, H. Zheng and Y. Liang, Molecular Catalyst with Near 100% Selectivity for CO_2 Reduction in Acidic Electrolytes, *Adv. Energy Mater.*, 2023, **13**, 1614-6832.

21. G. Zhang, Z.-J. Zhao, D. Cheng, H. Li, J. Yu, Q. Wang, H. Gao, J. Guo, H. Wang, G. A. Ozin, T. Wang and J. Gong, Efficient CO_2 electroreduction on facet-selective copper films with high conversion rate, *Nat. Commun.*, 2021, **12**, 5745.

22. M. Schreier, L. Curvat, F. Giordano, L. Steier, A. Abate, S. M. Zakeeruddin, J. Luo, M. T. Mayer and M. Grätzel, Efficient photosynthesis of carbon monoxide from CO_2 using perovskite photovoltaics, *Nat. Commun.*, 2015, **6**, 7326.

23. J. Gao, J. Li, Y. H. Liu, M. Xia, Y. Z. Finfrock, S. M. Zakeeruddin, D. Ren and M. Grätzel, Solar reduction of carbon dioxide on copper-tin electrocatalysts with energy conversion efficiency near 20%, *Nat. Commun.*, 2022, **13**, 5898.

24. J. Gao, H. Zhang, X. Guo, J. Luo, S. M. Zakeeruddin, D. Ren and M. Grätzel, Selective C–C Coupling in Carbon Dioxide Electroreduction via Efficient Spillover of Intermediates As Supported by Operando Raman Spectroscopy, *J. Am. Chem. Soc.*, 2019, **141**, 18704-18714.

25. Z. Chen, T. Wang, B. Liu, D. Cheng, C. Hu, G. Zhang, W. Zhu, H. Wang, Z.-J. Zhao and J. Gong, Grain-Boundary-Rich Copper for Efficient Solar-Driven Electrochemical CO_2 Reduction to Ethylene and Ethanol, *J. Am. Chem. Soc.*, 2020, **142**, 6878-6883.

26. D. Ren, N. W. X. Loo, L. Gong and B. S. Yeo, Continuous Production of Ethylene from Carbon Dioxide and Water Using Intermittent Sunlight, *ACS Sustain. Chem. Eng.*, 2017, **5**, 9191-9199.

27. B. Kim, H. Seong, J. T. Song, K. Kwak, H. Song, Y. C. Tan, G. Park, D. Lee and J. Oh, Over a 15.9% Solar-to-CO Conversion from Dilute CO_2 Streams Catalyzed by Gold Nanoclusters Exhibiting a High CO_2 Binding Affinity, *ACS Energy Lett.*, 2020, **5**, 749-757.

28. W.-H. Cheng, M. H. Richter, I. Sullivan, D. M. Larson, C. Xiang, B. S. Brunschwig and H. A. Atwater, CO_2 Reduction to CO with 19% Efficiency in a Solar-Driven Gas Diffusion Electrode Flow Cell under Outdoor Solar Illumination, *ACS Energy Lett.*, 2020, **5**, 470-476.

29. M. Schreier, F. Heroguel, L. Steier, S. Ahmad, J. S. Luterbacher, M. T. Mayer, J. Luo and M. Gratzel, Solar conversion of CO_2 to CO using Earth-abundant electrocatalysts prepared by atomic layer modification of CuO, *Nat. Energy*, 2017, **2**.